



Article

Thermal Discharge Temperature Retrieval and Monitoring of NPPs Based on SDGSAT-1 Images

Wenwen Huang ^{1,2} , Jingjie Jiao ^{1,2}, Lixing Zhao ^{1,2}, Zhuoyue Hu ³, Xiaohong Peng ^{2,3}, Lan Yang ^{2,3}, Xiaoyan Li ^{1,*} and Fansheng Chen ^{1,3,4}

¹ Hangzhou Institute for Advanced Study, University of Chinese Academy of Sciences, Hangzhou 310024, China

² University of Chinese Academy of Sciences, Beijing 100049, China

³ State Key Laboratory of Infrared Physics, Shanghai Institute of Technical Physics, Chinese Academy of Sciences, 500 Yu Tian Road, Shanghai 200083, China

⁴ International Research Center of Big Data for Sustainable Development Goals (CBAS), Beijing 100094, China

* Correspondence: lixiaoyan@ucas.ac.cn

Abstract: High-accuracy sea surface temperature (SST) retrieval near nuclear power plants (NPPs) is one of the most significant indicators for evaluating marine ecological environment quality, monitoring the real-time situation of thermal discharge, and supporting planning decisions. However, complex computations, the inaccessible real-time vertical profile of the atmosphere, and the uncertainty of atmospheric profile data increase the error of SST retrieval. Additionally, influenced by their low spatial resolution, the widely used AVHRR/MODIS remote sensing images (RSIs) are unable to retrieve the detailed distribution of SST in small scale regions such as coastal NPPs. In this paper, we propose a simplified split-window-based temperature retrieval method (the SW method) suitable for SDGSAT-1 30 m thermal infrared spectrometer (TIS) RSIs. Specially, this method only needs atmospheric transmittance and surface emissivity by counteracting the average atmospheric temperature to monitor the thermal discharge of offshore NPPs. First, the geometric and radiometric calibrated thermal infrared and multi-spectral cloudless data of the target regions are selected to obtain the corresponding apparent radiance of the RSIs. Second, in accordance with the red and near-infrared (NIR) bands of multi-spectral RSIs, the surface emissivity is calculated to distinguish water from land. Next, we determine the atmospheric profile parameters from the weather conditions of the target region at the imaging time. Finally, according to the theory of surface-atmosphere radiative transfer, the SST of target regions is retrieved with the proposed SW method, and the results are compared with those of the conventional radiative transfer equation (RTE), mono-window (MW), and the nonlinear sea surface temperature (NLSST) algorithms. The experimental results indicate that the SST retrieved from the split-window algorithms (i.e., SW and NLSST) are generally higher than those of the single-channel algorithms (i.e., RTE and MW). The SST difference between the SW algorithm and the NLSST algorithm is within 0.5 °C. In addition, SDGSAT-1 can monitor the seasonal detailed variation of the thermal discharge near coastal NPPs. This article is the first to attempt to quantitative small-scale SST retrieval based on thermal infrared and multi-spectral images obtained from the SDGSAT-1 TIS and a multispectral imager (MII), and therefore, provide an effective reference for marine environment monitoring.

Keywords: SST retrieval; the split-window algorithm; thermal infrared; thermal discharge



Citation: Huang, W.; Jiao, J.; Zhao, L.; Hu, Z.; Peng, X.; Yang, L.; Li, X.; Chen, F. Thermal Discharge Temperature Retrieval and Monitoring of NPPs Based on SDGSAT-1 Images. *Remote Sens.* **2023**, *15*, 2298. <https://doi.org/10.3390/rs15092298>

Academic Editor: Yi Luo

Received: 22 February 2023

Revised: 15 April 2023

Accepted: 25 April 2023

Published: 27 April 2023



Copyright: © 2023 by the authors. Licensee MDPI, Basel, Switzerland. This article is an open access article distributed under the terms and conditions of the Creative Commons Attribution (CC BY) license (<https://creativecommons.org/licenses/by/4.0/>).

1. Introduction

The rapid development of nuclear power has alleviated the greenhouse effect resulting from traditional thermal power fuels, but the marine thermal pollution caused by the transfer of waste heat from nuclear power plants (NPPs) cannot be ignored [1]. Sea surface temperature (SST) refers to the seawater temperature below the ocean surface with a

depth of less than 0.5 m [2,3], which is one of the important indicators used to evaluate an ecological environment [4]. The thermal discharge from NPPs influences SST which could increase dramatically and cause the death of fish, coral, and other coastal organisms [5]. Retrieval of SST has been of great importance in thermal contamination monitoring and has also become conducive to protecting the marine environment and maintaining ecological balance [6].

Many investigations and studies on monitoring and evaluating thermal discharge near NPPs have been conducted based on field observations [7] and satellite remote sensing technology [6,8]. Due to the restricted direct-measure range and limited number of discrete oceanographic stations, conducting dynamic and successive thermal discharge monitoring through high-cost field observations is challenging, which significantly hinders intuitively displaying the spatiotemporal variation of thermal discharge. Satellite remote sensing technology provides a new means for monitoring the thermal discharge of NPPs by detecting the sea's surface thermal radiation and calculating the SST indirectly. Compared with a single field-based measurement, satellite remote sensing technology has the advantages of abundant global data, fast update speed, and wide spatiotemporal monitoring range. According to the electromagnetic wavelength of the data, satellite remote sensing technology can be divided into microwave [9] and infrared remote sensing [10], as shown in Table 1. Although microwave remote sensing can penetrate the clouds to obtain sea surface radiation, the low spatial resolution and underdeveloped retrieval algorithms significantly limit its application. SST retrieval based on infrared remote sensing can reduce costs and improve the efficiency of thermal discharge monitoring, as well as intuitively display the spatial diffusion and temporal variability of the thermal discharge.

Table 1. Remote sensing data for SST retrieval.

Items	Payloads	Wavelength	Revisit	Resolution
Microwave	FY-3B MWRI	10.65/18.7/23.8/36.5/89.0 GHz	1 day	15–85 km
	TRMM TMI	10.7/19.4/21.3/37.0/85.5 GHz	1–2 days	25–50 km
	GCOM-W1 AMSR2	6–89 GHz	1–3 days	31.25 km
	DMSP SSM/I	19.36/22.23/37.0/85.5 GHz	1 day	12.5–25 km
Infrared	GOES ABI	10.5–12.5 μm	0.5–1 h	3–10 km
	FY2S VISSR	10.3–11.3/11.5–12.5 μm		
	Terra MODIS	10.78–11.28/11.77–12.27 μm	12 h	1 km
	NOAA AVHRR	10.3–11.3/11.5–12.5	12 h	1.1 km
	ERS-2 ATSR-2	10.35–11.35/11.5–12.5 μm	1–2 days	1–2 km
	FY-3 VIRR	10.3–11.3/11.5–12.5 μm	1–4 days	1.1 km
	Sentinel-3 SLSTR	10.8–12.02 μm	2 days	1 km
	S-NPP VIIRS	8–12 μm	16 days	750 m
	Landsat-7 ETM+	10.4–12.5 μm	1–16 days	
	Landsat-8 TIRS	10.6–11.19/11.5–12.51 μm	16 days	100 m
Terra ASTER	8.125–8.475/8.475–8.825/8.925–9.275/10.25–10.95/10.95–11.65 μm	16 days	90 m	

So far, a large number of thermal infrared remote sensing images (RSIs) have been widely used for surface temperature retrieval such as moderate-resolution imaging spectroradiometer (MODIS) [11], advanced very high resolution radiometer (AVHRR) [12], and Landsat-8 thermal infrared sensor (TIRS) [13] images. MODIS and AVHRR data are pioneers in achieving mass production of free SST products on websites, which have become the underlying supporting data in the world. Tang examined AVHRR SST and shipboard measurements of the thermal plume from the Daya Bay [7]. Nie employed higher resolution Landsat data to monitor the thermal discharge near the Tianwan NPP [14]. However, frequent cloud coverage [15], missing strip photograph, and low temporal resolution can severely affect the actual effect of thermal discharge dynamic monitoring. Cloud coverage creates many difficulties for subsequent target detection and identification, and also directly reduces the accuracy of surface temperature retrieval.

According to the band number and characteristics of infrared RSIs, researchers have proposed a variety of surface temperature retrieval algorithms [16–19] which can be divided into two categories: single-channel algorithms such as the radiative transfer equation (RTE) algorithm [20,21] and the mono-window (MW) algorithm [22,23], and multi-channel algorithms such as the split-window algorithm [24,25] and the nonlinear sea surface temperature (NLSST) algorithm [12,26]. In 2001, according to the surface heat radiation conduction equation, Qin linearized the Planck function and put forward an MW algorithm [27] that simplified the calculation of the upward and downward atmospheric radiation and was applied to SST retrieval of Landsat TM6 thermal infrared RSIs. Chen evaluated and compared the performance of the RTE and MW algorithms [22,27,28] on SST retrieval from Landsat-8 TIRS RSIs in the coastal water of the Hongyan River NPP [28]. Considering various atmospheric influences, the RTE method is the most comprehensive and rational algorithm, but the complex computation, inaccessible real-time atmospheric vertical profile, and uncertainty of atmospheric profile parameters increase the error of SST retrieval. Jimenez-Munoz proposed a generalized single-channel method that depended only on the vapor content [23]. In terms of AVHRR, McMillin proposed a two-channel linear correction method, namely the split-window algorithm, to obtain the SST quantitatively by eliminating atmospheric influence [25,29]. Subsequently, associated scholars have put forward many improved, different types of split-window algorithms according to the surface heat radiation conduction equation and the discrepant atmospheric absorption theory of the split-window channels. In 2020, Fu proposed a new split-window algorithm for retrieving SST from Landsat-8 TIRS thermal infrared RSIs based on the variation of atmospheric water vapor content [24]. Additionally, multi-channel algorithms also include the day/night algorithm for MODIS data and the temperature emissivity separation algorithm applicable for ASTER RSIs [13,30,31].

With the expansion of maritime military and civil demands, people’s requirements for SST detailed distribution in small scale regions are increasingly stringent and it is especially urgent to manufacture high-resolution SST retrieval products [32]. Aiming at elaborating the interaction between human activities and the natural environment, SDGSAT-1 was launched in November 2021, with the core payloads being a thermal infrared spectrometer (TIS) and a multispectral imager (MII) that can acquire three spectral thermal infrared images and multispectral RSIs of the Earth’s surface at an orbit altitude of 505 km to provide higher precision, dynamic, multi-scale, and periodic rich information for SST retrieval. The detailed specifications of the TIS and MII are shown in Table 2. To achieve fine monitoring of thermal discharge of NPPs, in this paper, we propose a simplified split-window-based temperature retrieval method (SW) suitable for SDGSAT-1 30 m TIS RSIs. Specially, this method only requires atmospheric transmittance and surface emissivity by counteracting the average atmospheric temperature to monitor the thermal discharge of offshore NPPs.

Table 2. Technical and performance index of the SDGSAT-1 TIS and MII.

Payloads	Spectrum (μm)	Resolution (m)	NETD/SNR	Radio-Calibration Precision
TIS	B1:8–10.5 B2:10.30–11.3 B3:11.5–12.5	30	0.2 K@300 K	Relative: 5% Absolute: 1 K@300 K
MII	b1:0.374–0.427 b2:0.410–0.467 b3:0.457–0.529 b4:0.510–0.597 b5:0.618–0.696 b6:0.744–0.813 b7:0.798–0.911	10	≥ 130 ≥ 150	Relative: 2% Absolute: 5%

The remainder of this paper is organized as follows: First, in Section 2, we describe the methodology for thermal discharge monitoring including data preprocess (geometric and radiometric calibration), surface emissivity calculation, atmospheric transmissivity calculation, and four different SST retrieval algorithms (RTE, MW, SW, and NLSST). In Section 3, we analyze and discuss the experimental results from the four algorithms. Then, we conclude the methods and its application in Section 4. Finally, some interferences in SST retrieval and the prospects for future optimization are pointed out.

2. Methodology

SST retrieval is one of the indispensable steps in the study of thermal effluent distribution. In this section, we introduce the conventional RTE, MW, and NLSST algorithms and we propose the SW method based on 30 m TIS thermal infrared RSIs and 10 m MII multi-spectral images of SDGSAT-1, as shown in Figure 1. First, the thermal infrared and multi-spectral cloudless RSIs of the target regions after geometric and radiometric calibration are selected to obtain the corresponding apparent radiance of the RSIs. Second, in accordance with the red and near-infrared (NIR) bands of multi-spectral data, surface emissivity is calculated to distinguish water from land. Then, we determine the atmospheric profile parameters from the weather conditions of the target region at the imaging time. Finally, according to the theory of surface-atmosphere radiative transfer, the SST of target regions is retrieved using the four methods mentioned above.

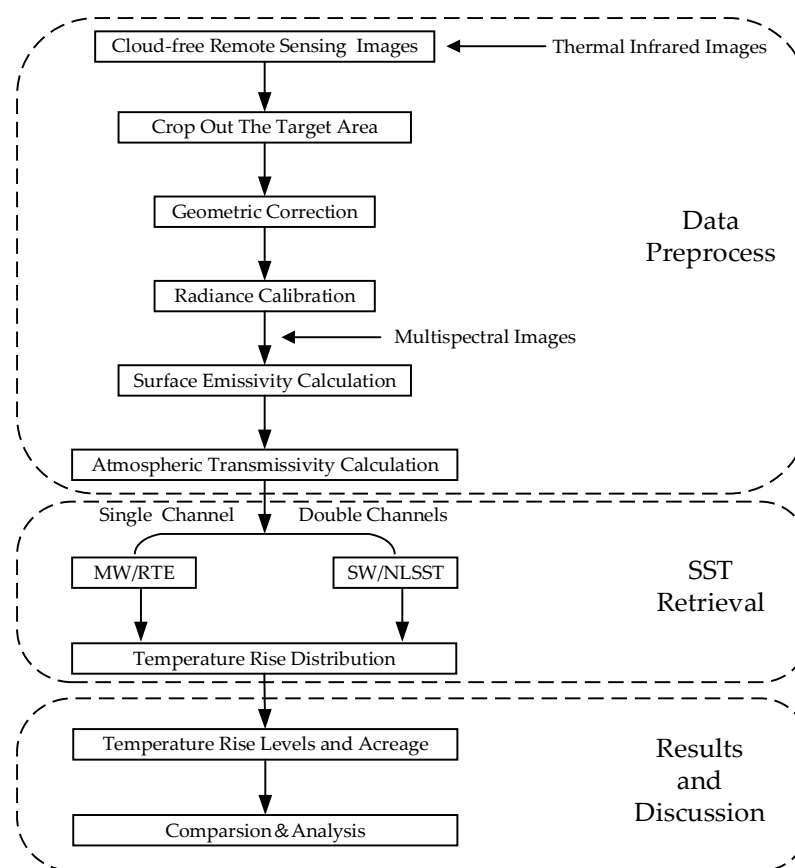


Figure 1. Flowchart of the thermal discharge temperature retrieval and monitoring of the NPPs.

2.1. Data Preprocess

2.1.1. Geometric Correction

The cloudless images covering the target NPPs should be geometrically corrected based on the ground control points or digital elevation model, and the small geometric positioning error will be helpful for subsequent processing. In this paper, the geometric

correction process for the SDGSAT-1 TIS/MII and Landsat-8 TIRS RSIs employed in the experiment had been previously completed [15,33].

2.1.2. Radiometric Calibration

Ground objects at different temperatures are reflected on the obvious gray discrepancy in the infrared images. As shown in Equation (1), the apparent radiance L_λ of thermal infrared and multi-spectral images can be calculated by using the calibration coefficients provided by the official website:

$$L_\lambda = \text{gain} \times \text{DN} + \text{bias} \quad (1)$$

where gain and bias, respectively, represent the absolute calibration gain and offset, and can be obtained from the meta-files, as shown in Table 3. DN is the gray value of the pixels. The temperature (T) of thermal infrared images can be deduced from Planck' law [34], as shown in Equation (2):

$$T = \frac{k_2}{\ln \left[\frac{k_1}{L_\lambda(T)} + 1 \right]} \quad (2)$$

where k_1 and k_2 are the specific thermal conversion coefficients depending on the wavelength $\lambda(\mu\text{m})$, as shown in Table 3.

Table 3. Parameters for the radiometric calibration of the TIS/MII/TIRS.

Parameters	TIS-B1	TIS-B2	TIS-B3	TIRS-B10	TIRS-B11	MII-Red	MII-NIR
gain	0.003947	0.003946	0.005329	0.000342	0.000342	0.016096	0.019719
bias	0.167126	0.124622	0.222530	0.1	0.1	0	0
k_1	1655.628	838.706	543.058	774.89	480.89		
k_2	1542.762	1342.719	1232.021	1321.08	1201.14		

2.2. Surface Emissivity Calculation

Surface emissivity (ϵ) is one of the most important parameters in earth surface temperature retrieval [35], which affects the radiation emitted from the Earth's diverse surface. The emissivity of a surface mainly depends on the material structure of the target surface, the spectral range of the detector, and the pixel resolution. Surface emissivity varies slightly with the wavelength and can be replaced by the surface emissivity at the channel's central wavelength. Generally, the Earth's surface can be divided into water, towns, and bare land, and their emissivity can be calculated by using the NDVI threshold method as Equations (3)–(5) [13,36]. The spectral characteristics of water are obviously distinct from others, whose surface emissivity can be estimated as 0.995 in surface temperature retrieval (8–12 μm). Compared to land surface temperature retrieval, water pixels account for a larger proportion in SST retrieval. Water-land separation is employed in SST retrieval to independently retrieve the water surface temperature. For areas that are easily affected by tides, the NDVI threshold method is often used for water-land separation. For areas that are not easily affected by tides, the water surface can be directly extracted according to fixed shoreline boundaries.

$$\begin{cases} \epsilon_{\text{water}} = 0.995 \\ \epsilon_{\text{towns}} = 0.9589 + 0.086 \times F_v - 0.0671 \times F_v \times F_v \\ \epsilon_{\text{bare-land}} = 0.9625 + 0.0614 \times F_v - 0.0461 \times F_v \times F_v \end{cases} \quad (3)$$

$$F_v = \left[\frac{\text{NDVI} - \text{NDVI}_{\min}}{\text{NDVI} - \text{NDVI}_{\max}} \right]^2 \quad (4)$$

$$\text{NDVI} = \frac{P(\text{Red}) - P(\text{NIR})}{P(\text{Red}) + P(\text{NIR})} \quad (5)$$

where F_v is the fractional vegetation. NDVI is the normalized difference vegetation index and can be deduced from Equation (5). $NDVI_{\min/\max}$ is the minimum/maximum of NDVI in the target region, which represents the pure soil/vegetation. Generally, $NDVI_{\min} = 0.05$ and $NDVI_{\max} = 0.7$. P is the pixel value of the radiometric calibrated red/NIR images and can be calculated using Equation (1).

2.3. Atmospheric Transmissivity Calculation

Atmospheric transmissivity, which is affected by fluctuations in meteorological conditions such as atmospheric pressure, humidity, and gas density, can change significantly, and therefore, can have an obvious impact on infrared radiation transmission [37] and the accuracy of SST retrieval. In view of the difficulties in obtaining real-time atmospheric profile data, researchers have typically used MODTRAN, LOWTRAN, 6S, and other software to simulate atmospheric transmittance τ [37]. For the MODIS, NIR images (B2/B19) can be used to retrieve atmospheric water vapor content w (g/cm^2); thus, some researchers have also estimated τ by simulating the relationship between w and the band-31/32 atmospheric transmissivity $\tau_{31/32}$, as shown in Equations (6) and (7) [38]:

$$w = [0.02 - \ln(\text{ref}_{19}/\text{ref}_2)]/0.651 \quad (6)$$

$$\begin{cases} \tau_{31} = 5.72 - 4.69e^{w/42.05}, R^2 = 1.00 \\ \tau_{31} = -1.25 + 2.28e^{-w/12.44}, R^2 = 0.99 \end{cases} \quad (7)$$

where $\text{ref}_{19/2}$ is the band-19/2 surface emissivity of MODIS.

2.4. SST Retrieval

In the process of surface-atmosphere radiative transfer [39], the thermal energy mainly radiates outward through two atmospheric windows: 3–5 μm and 8–14 μm [40]. The energy received by a thermal infrared sensor includes three parts: the surface heat radiation after atmospheric weakening, the upward atmospheric radiation received by the sensor, and the surface-reflecting energy of the downward atmospheric radiation. Therefore, the apparent radiance of RSIs is inevitably affected by surface temperature, surface emissivity, and atmospheric transmission. Due to the influence of atmospheric absorption (especially, water and gas absorption) and scattering, the total radiation received by the sensor does not reflect the true radiation of the Earth's surface, and therefore, atmospheric correction is used to eliminate these radiation errors. It is necessary for SST retrieval to remove the atmospheric radiation from thermal infrared RSIs to obtain the real reflectance, radiation, and temperature of the surface. Surface temperature retrieval is essentially a type of special atmospheric correction.

2.4.1. RTE Algorithm

Considering the various atmospheric influences, the RTE method is the most comprehensive and rational algorithm. Assuming that there is uniform atmosphere without cloud interference, when the actual surface temperature is T_S (K), the top atmospheric radiation obtained by the thermal infrared imager is the apparent radiance L_λ , which is composed of the upward atmospheric radiance $L_{\lambda\text{atm}\uparrow}$, the energy $\varepsilon_\lambda \tau_\lambda L_\lambda(T_S)$ from the actual ground radiance passing through the atmosphere and finally reaching the detector, and the reflected energy of the downward radiance $(1 - \varepsilon_\lambda) \tau_\lambda L_{\lambda\text{atm}\downarrow}$. The corresponding blackbody radiation $L_\lambda(T_S)$ of the object is as shown in Equation (8) and the actual surface temperature T_S can be obtained by using Equation (2):

$$L_\lambda(T_S) = \frac{L_\lambda - L_{\lambda\text{atm}\uparrow}}{\varepsilon_\lambda \tau_\lambda} - \frac{(1 - \varepsilon_\lambda) L_{\lambda\text{atm}\downarrow}}{\varepsilon_\lambda} \quad (8)$$

where ε_λ is the surface emissivity and τ_λ is the atmospheric transmissivity. $L_{\lambda\text{atm}\downarrow}$ is the downward atmospheric radiance. In order to obtain the actual surface temperature T_S by

employing the RTE algorithm, the surface specific emissivity ϵ_λ , atmospheric transmittance τ_λ , $L_{\lambda\text{atm}\uparrow}$, and $L_{\lambda\text{atm}\downarrow}$ should be estimated in advance. The abovementioned atmospheric parameters can be simulated in MODTRAN if the air temperature, pressure, relative humidity, elevation, and other meteorological data are known.

2.4.2. MW Algorithm

The MW algorithm can avoid calculation of the upward and downward atmospheric radiation, according to Qin [27]. The calculation formula of the MW algorithm is shown as Equation (9):

$$T_S = \{a(1 - C - D) + T_{\text{sensor}}[b(1 - C - D) + C + D] - DT_{\text{ave}}\}/C \quad (9)$$

where T_S is the actual surface temperature (K). T_{sensor} is the brightness temperature, which can be obtained by Equation (2). The coefficients a and b should be modified according to the spectral response function if the spectrum changes. When $0^\circ\text{C} \leq T_S \leq 70^\circ\text{C}$, $a = -66.2795$, $a = -66.2795$ and $b = 0.4461$ for Landsat-8 TIRS band-10 (10.60~11.19 μm) RSIs. $C = \epsilon_\lambda\tau_\lambda$, $D = (1 - \tau_\lambda)[1 + (1 - \epsilon_\lambda)\tau_\lambda]$ are the intermediate variables. ϵ_λ is the surface emissivity and τ_λ is the atmospheric transmissivity. T_{ave} is the average atmospheric temperature (K), which can be divided into three cases: tropic, summer in mid-latitudes, and winter in mid-latitudes, as shown in Equation (10). The temperature near the ground (T_0) is usually replaced by the brightness temperature. The MW algorithm needs to calculate the brightness temperature (T_{sensor}), surface emissivity (ϵ_λ), and atmospheric transmissivity (τ_λ) to obtain the actual surface temperature T_S :

$$\begin{cases} T_{\text{ave-summer}} = 16.0110 + 0.92621T_0 \\ T_{\text{ave-winter}} = 19.2704 + 0.91118T_0 \\ T_{\text{tropic}} = 17.9769 + 0.91715T_0 \end{cases} \quad (10)$$

2.4.3. SW Algorithm

The split-window algorithm, applied mainly for AVHRR SST retrieval, can correct the atmospheric radiation through the combination of two adjacent thermal infrared channels with obviously different atmospheric absorption [41,42]. Currently, there are nearly twenty publicly published split-window algorithms and their basic form is shown as Equation (11), representing surface temperature through a linear/nonlinear combination of brightness temperatures in multiple bands [16]:

$$T_S = A_0 + A_1T_i + A_2T_j \quad (11)$$

where T_S (K) is the actual surface temperature; T_i , T_j are, respectively, the brightness temperature of band- i and band- j ; A_0 , A_1 , A_2 are the parameters determined by the atmospheric transmissivity and surface emissivity.

SDGSAT-1 TIS, containing three thermal infrared bands with a spatial resolution of 30 m, has the advantages of more thermal channels and higher spatial resolution which is suitable for surface temperature retrieval in the offshore sea. The brightness temperature difference between TIS B2 and B3 of forty samples are calculated by using Equations (1) and (2). As shown in Figure 2a, there are seven samples less than zero and thirty-three samples greater than zero. It is obvious that the radiation of the two adjacent bands is actually different. In this paper, we select the TIS B2 images as the data source for the RTE and MW algorithms and take the combination of the TIS B2 and B3 images as the input for the SW and NLSST algorithms.

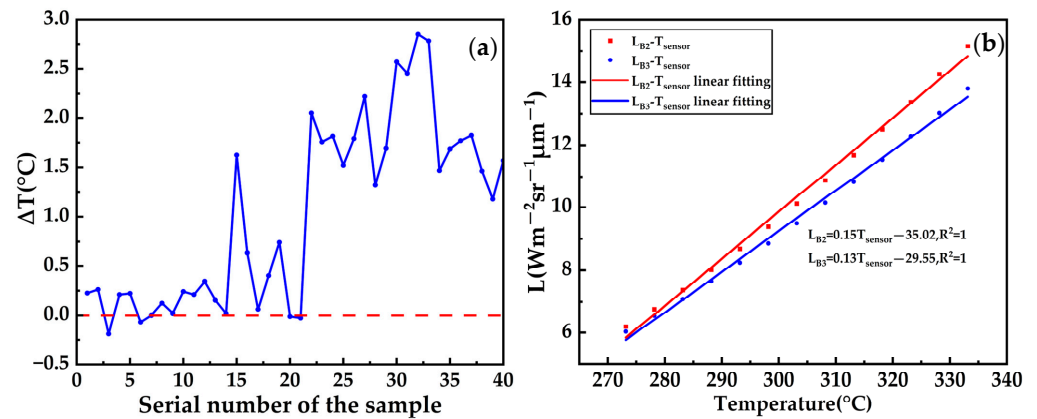


Figure 2. (a) The brightness temperature difference between TIS B2 and B3; (b) the linear fitting between the temperature and radiance for TIS B2 and B3.

The SW algorithm that is suitable for SDGSAT-1 images is derived as shown in Figure 3, which needs fewer parameters and facilitates its quantitative application by counteracting the average atmospheric temperature.

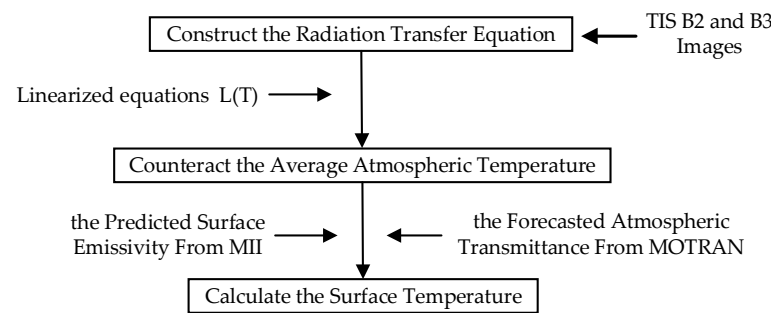


Figure 3. Flowchart of the SW algorithm for SDGSAT-1 images.

First, we construct the radiative transfer equation for TIS B2 and B3 images as Equation (12).

$$\begin{cases} L_2(T_2) = \epsilon\tau_2(\theta)L_2(T_S) + [1 - \tau_2(\theta)] \times [1 + (1 - \epsilon)\tau_2(\theta)]L_2(T_T) \\ L_3(T_3) = \epsilon\tau_3(\theta)L_3(T_S) + [1 - \tau_3(\theta)] \times [1 + (1 - \epsilon)\tau_3(\theta)]L_3(T_T) \end{cases} \quad (12)$$

where $T_2, T_3(K)$ are the brightness temperature of the TIS B2 and B3 RSIs, respectively. $T_S(K)$ is the actual surface temperature and $T_T(K)$ is the average atmospheric temperature. ϵ is the surface emissivity (8–12 μm) and $\tau_2(\theta), \tau_3(\theta)$ are the atmospheric transmissivity when the zenith angle of TIS is θ . $L_2(T_2), L_3(T_3)$ are the apparent radiance received by the sensor and $L_2(T_T), L_3(T_T)$ are the apparent radiance corresponding to the average atmospheric temperature. It is difficult to directly calculate the surface temperature because of the complex nonlinear properties of the Planck equation [34]. We provide the scatter plot between temperature and apparent radiance based on the TIS B2 and B3 images, as shown in Figure 2b. It is found that the relationship between temperature and apparent radiance is approximately linear in 0–50 °C, as Equation (13). Then, Equation (12) can be reduced to Equation (14) by counteracting T_T . Finally, T_S can be estimated only if ϵ and $\tau_2(\theta), \tau_3(\theta)$ are predicted according to Sections 2.2 and 2.3.

$$\begin{cases} L_2 = a_2T - b_2 = 0.15T - 35.02, R^2 = 1 \\ L_3 = a_3T - b_3 = 0.13T - 29.55, R^2 = 1 \end{cases} \quad (13)$$

$$T_s = \frac{M_3M_2(\frac{b_2}{a_2} - \frac{b_3}{a_3}) + M_3(a_2T_2 - b_2) - M_2(a_3T_3 - b_3) + Pb_2 - Qb_3}{(Pa_2 - Qa_3)} \quad (14)$$

$$\begin{cases} M_3 = \{a_3(1 - \tau_3)[1 + \tau_3(1 - \varepsilon)]\} \\ M_2 = \{a_2(1 - \tau_2)[1 + \tau_2(1 - \varepsilon)]\} \\ P = M_3\tau_2\varepsilon \\ Q = M_2\tau_3\varepsilon \end{cases} \quad (15)$$

where $a_2 = 0.15, b_2 = 35.02, a_3 = 0.13, b_3 = 29.55$ and M_2, M_3, P, Q are the intermediate parameters determined by the atmospheric transmissivity and surface emissivity.

2.4.4. NLSST Algorithm

The relative spectral response functions for different channels of the TIS, AVHRR, MODIS, and TIRS sensors are shown in Figure 4 and the setting of the two thermal infrared bands (B2: 10.30–11.3 μm and B3:11.5–12.5 μm) of SDGSAT-1 TIS is consistent with the CH4 (10.30–11.3 μm) and CH5 (11.5–12.5 μm) of NOAA AVHRR, as shown in Tables 1 and 2. The NLSST algorithm is specially designed for AVHRR CH4 and CH5. The SST results retrieved from the SSW algorithm should be theoretically similar to those of the NLSST algorithm for the same RSIs.

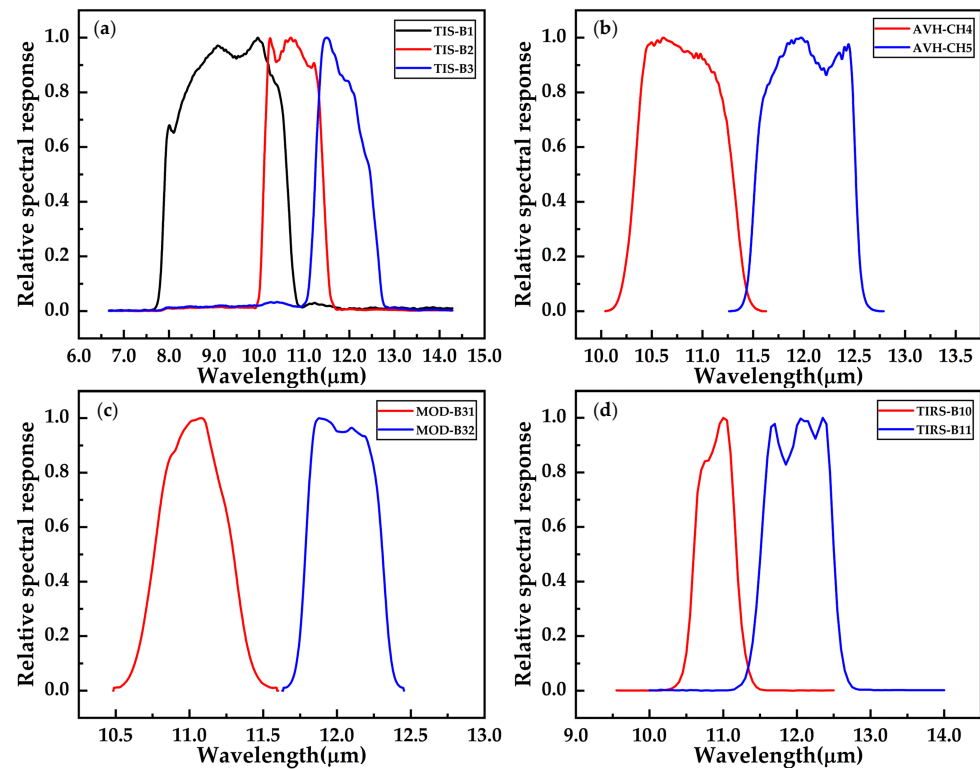


Figure 4. The relative spectral response function for different channels of the sensors: (a) TIS-B1/B2/B3; (b) AVHRR-CH4/CH5; (c) MODIS-B31/B32; (d) TIRS-B10/B11.

Here, we take the NLSST algorithm [12] as a contrast to evaluate the accuracy of the SW algorithm, as Equation (16):

$$T_S = C_1T_4 + C_2(T_4 - T_5) + C_3(T_4 - T_5)(\sec\theta - 1) + C_4 \quad (16)$$

where $T_S(\text{K})$ is the actual surface temperature and T_4, T_5 are the brightness temperature (K) of the AVHRR CH4 and CH5 RSIs, respectively. θ is the zenith angle of the sensor. $c_1 = 1.0222, c_2 = 2.31, c_3 = 0.83, c_4 = -280.39$, which are regressed by the drifting and fixed buoys data in the tropical Pacific.

3. Results and Discussion

3.1. Experimental Data

In this study, the Tianwan (TW), Ling'ao (LA), Yangjiang (YJ), and Hongyan River (HY) NPPs and their adjacent sea areas are taken as our experimental areas, and their geographical distribution is shown in Figure 5. The TW NPP, located in Lianyungang City, Jiangsu Province, is the largest single capacity NPP which can accommodate eight nuclear power generation units in the order of megawatts with a total installed capacity of 8–10 million kilowatts and an annual power generation of 60–70 billion kilowatt hours. The LA NPP is China's first large commercial NPP with a total of six megawatt class pressurized water reactor nuclear power units, located in Dapeng New District, Shenzhen City, Guangdong Province. It has an annual generating capacity of about 45 billion kilowatt hours. The YJ NPP, located in Dongping Town, Yangjiang City, Guangdong Province, is the only private NPP in southern China with a total installed capacity of 1100 megawatts. The HY NPP, located in Hongyan River Town, Wafangdian City, Liaoning Province, is the first NPP in northeast China with a total of six million kilowatts pressurized water reactor nuclear power units.

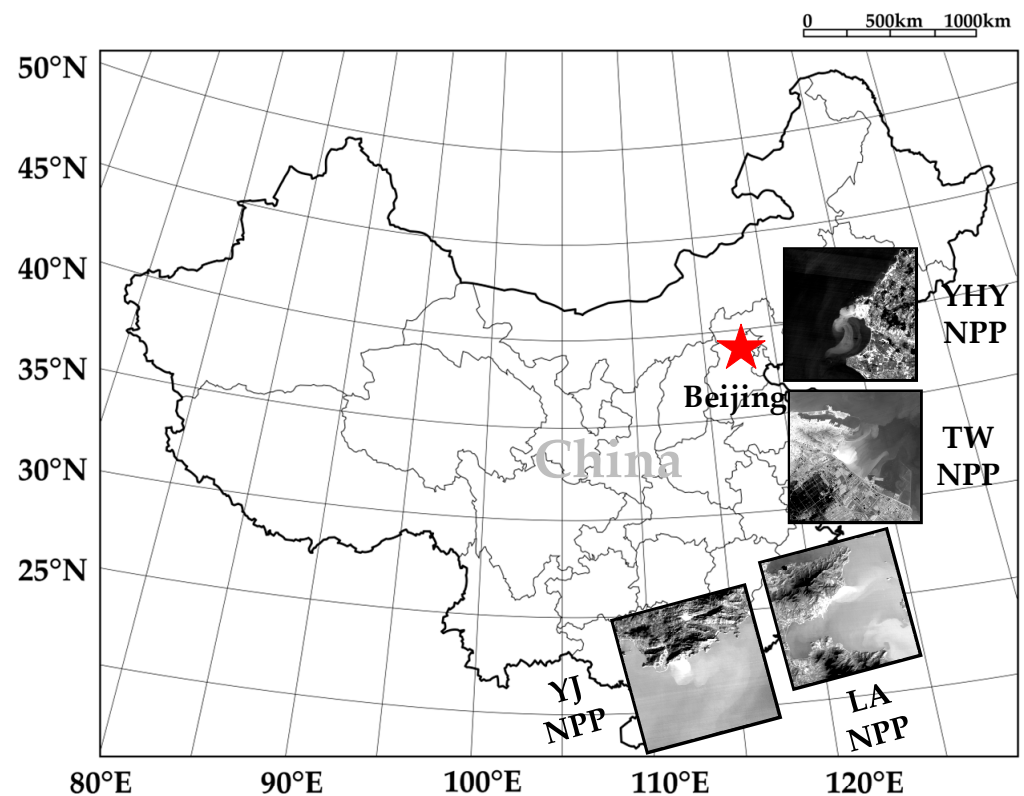


Figure 5. The geographical distribution of the experimental data.

Eighteen TIS images and thirteen MII images, with less than 5% cloud cover, of the four NPPs are selected and the corresponding Landsat-8 TIRS images in the same place are picked out as the contrast. The images' detailed information is shown in Table 4 and all the experimental images have been geometric corrected and cropped to the same size (1000 pixels \times 1000 pixels). 'Image Name' in Table 4 is in the form 'NPP-sensor-time'. 'TW-TIS-220517' represents the TIS image of the Tianwan Nuclear Power Plant taken on 17 May 2022.

Table 4. Detailed information about the selected images.

Regions	Image Name	Acquisition Time	Solar Zenith Angle (°)
TW NPP	TW-TIS-220517	21:17	113.602
	TW-TIS-220615	09:54	29.476
	TW-TIS-220625	10:03	29.749
	TW-TIS-220911	10:02	41.492
	TW-TIS-230111	09:56	64.582
	TW-TIS-230127	09:54	61.806
	TW-MII-220504		
	TW-MII-220615		
	TW-MII-220625		
	TW-MII-220911		
	TW-MII-230111		
	TW-MII-230127		
	TW-TIRS-200526	08:36	
LA NPP	LA-TIS-220307	21:46	135.027
	LA-TIS-220625	10:06	31.078
	LA-TIS-220712	21:45	120.520
	LA-TIS-221221	10:14	56.250
	LA-MII-220625		
	LA-MII-221221		
	LA-TIRS-211230	10:46	
YJ NPP	YJ-TIS-220722	21:52	122.796
	YJ-TIS-220827	21:59	130.618
	YJ-TIS-221211	10:14	54.269
	YJ-MII-220406		
	YJ-TIRS-211212	10:59	
HY NPP	HY-TIS-220520	09:47	31.565
	HY-TIS-220629	21:01	104.302
	HY-TIS-220911	10:01	43.620
	HY-TIS-221117	09:48	63.627
	HY-TIS-230111	09:45	68.855
	HY-MII-220520		
	HY-MII-220911		
	HY-MII-221117		
	HY-MII-230111		
	HY-TIRS-211207	08:35	

3.2. Results and Discussion

In this paper, twenty-two thermal infrared RSIs that originated from the TIS/TIRS at the TW, LA, YJ, and HY NPPs are selected to quantitatively retrieve SST. As shown in Figure 1, first, we crop the selected images to obtain experimental images that fully cover the potential temperature rising area. Then, four SST retrieval algorithms (RTE, MW, NLSST, and SW) are employed to retrieve SST. Next, we grade the SST distribution and mark the temperature rise levels with different colors. Finally, we count the distribution acreage at every level.

The SST that is not affected by thermal pollution is called the datum T_0 . Objective and accurate T_0 is of great significance for evaluating the thermal contamination of NPPs and methods for obtaining T_0 must avoid the influence of potential thermal discharge. Additionally, T_0 should represent the average temperature in the measurement area at different times as much as possible. For open seas, SST in the same area before the NPPs' operation can be taken as T_0 . For semi-closed seas, the average SST of the area not polluted by thermal discharge can be used as T_0 . In this experiment, all four NPPs are semi-closed seas and the average SST of the area away from temperature rising area is defined as datum T_0 . After obtaining the SST and datum T_0 , the temperature rising area is determined. In this paper, we formulate the specification and mapping for temperature rise levels, as shown in

Table 5, and different colors are used to mark the temperature rise levels. According to the number of pixels occupied by each temperature rising level and the spatial resolution of RSIs, the distribution acreage and area proportions of different temperature rise levels can be derived.

Table 5. Specification and mapping for temperature rise levels.

Temperature Rise Levels	$\Delta T = T_S - T_0 (^{\circ}\text{C})$	R	G	B
Datum T_0	$\Delta T = 0$	40	40	204
L1	$0 < \Delta T \leq 1$	40	204	40
L2	$1 < \Delta T \leq 2$	204	149	40
L3	$2 < \Delta T \leq 3$	204	95	40
L4	$3 < \Delta T \leq 4$	204	40	40

3.2.1. SST Distribution

The SST retrieved from the SDGSAT-1 TIS and Landsat-8 TIRS images of the TW NPP, LA NPP, YJ NPP, and HY NPP are, respectively, displayed in Figures 6–9. It is obvious that the TIS images can depict more prominent boundary and clearer details than TIRS images because of higher spatial resolution (30 m). Considering that the distribution of thermal discharge is easily influenced by the season, tides, and geographical location, the multi-temporal and higher spatial-resolution TIS data are more suitable for describing the subtle changes in thermal discharge than that of Landsat-8 TIRS, MODIS, and AVHRR data. Therefore, TIS data are a better option for monitoring subtle variations in thermal discharge and for evaluating marine environments.

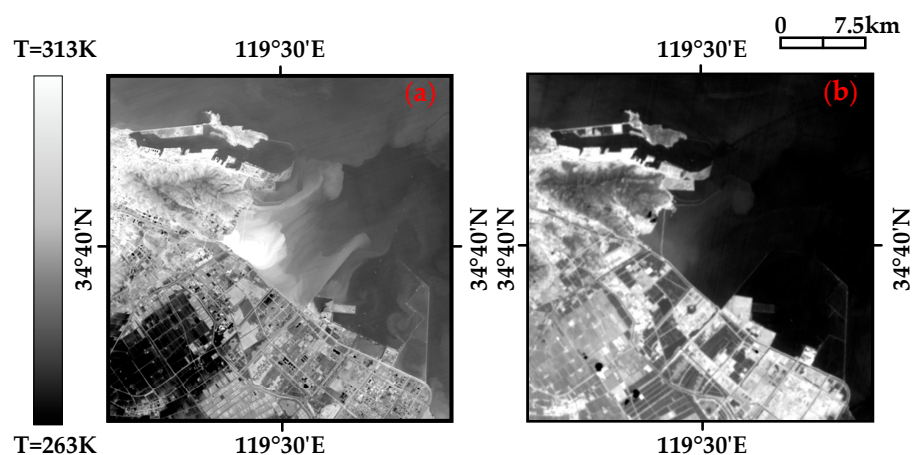


Figure 6. The retrieved SST from the TIS and TIRS images of the TW NPP: (a) TIS; (b) TIRS.

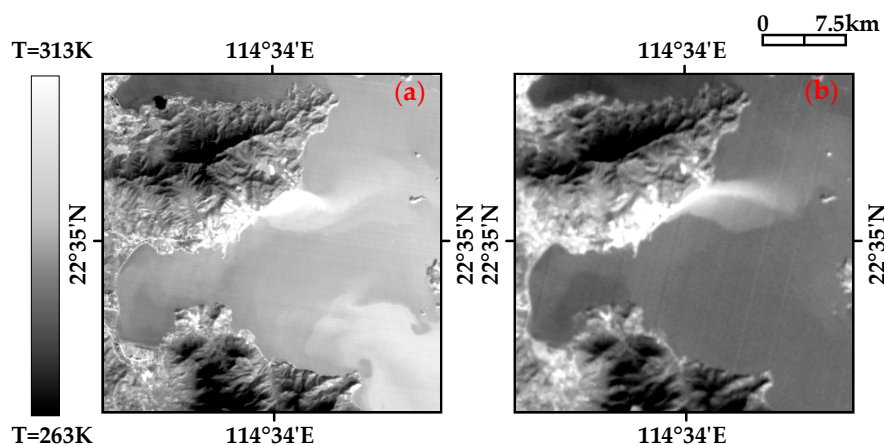


Figure 7. The retrieved SST from the TIS and TIRS images of the LA NPP: (a) TIS; (b) TIRS.

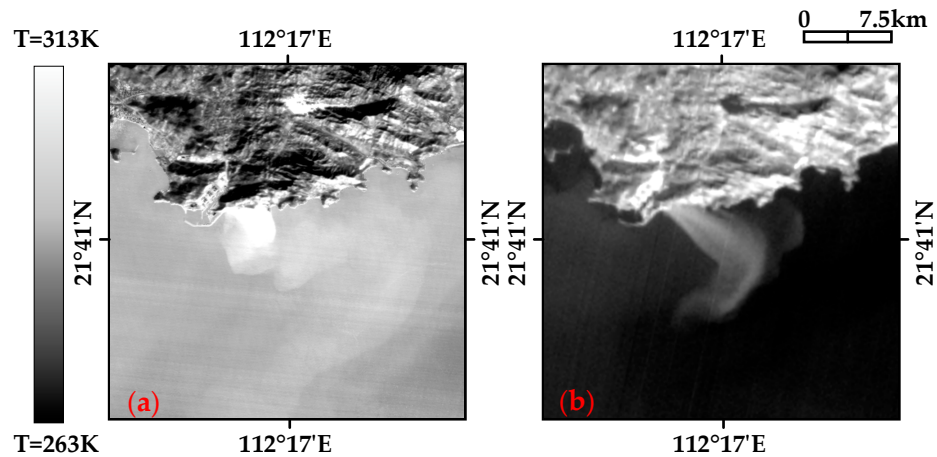


Figure 8. The retrieved SST from the TIS and TIRS images of the YJ NPP: (a) TIS; (b) TIRS.

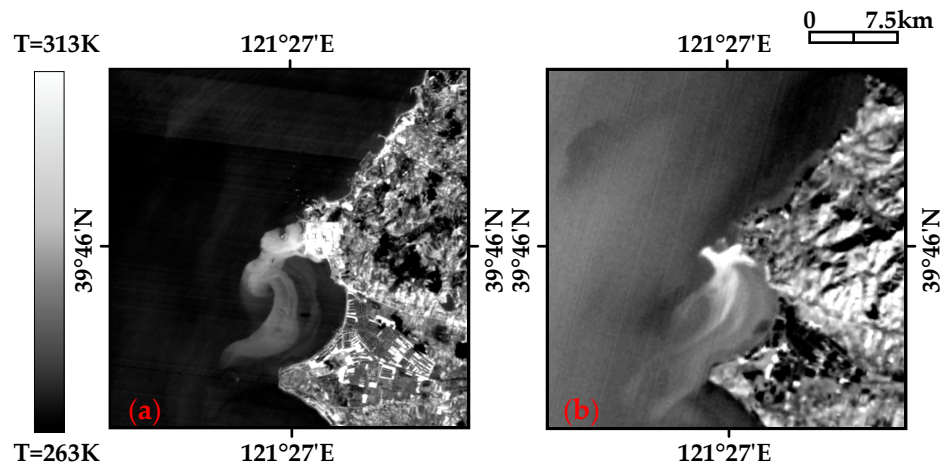


Figure 9. The retrieved SST from the TIS and TIRS images of the HY NPP: (a) TIS; (b) TIRS.

3.2.2. SST Comparison

In Figures 10–13, thirty-one points are uniformly sampled from the SST results retrieved from the TW NPP, LA NPP, YJ NPP, and HY NPP TIS images, respectively. The brightness temperature of B2 (B2-Tsensor), brightness temperature of B3 (B3-Tsensor), SST retrieved by the MW algorithm (MWSST), SST retrieved by the RTE algorithm (RTESST), SST retrieved by the NLSST algorithm (NLSST), and SST retrieved by the SW algorithm (SWSST) of the 31 sampling points are statistically shown in Figure 14.

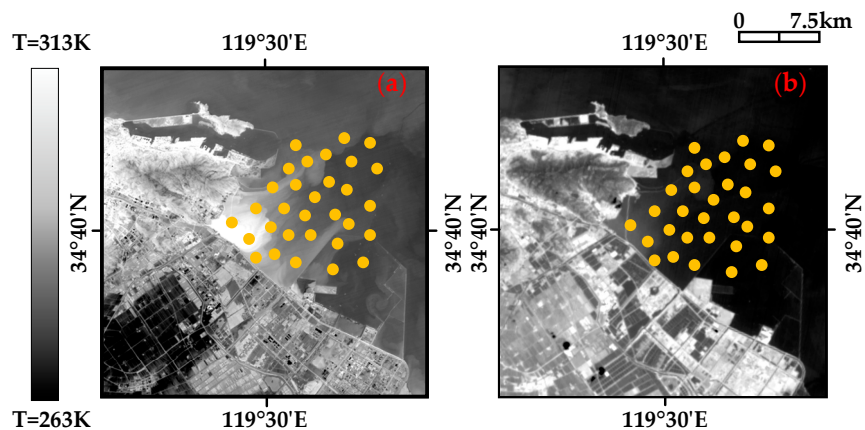


Figure 10. Spatial distribution of the 31 sampling points from the TW NPP: (a) TIS; (b) TIRS.

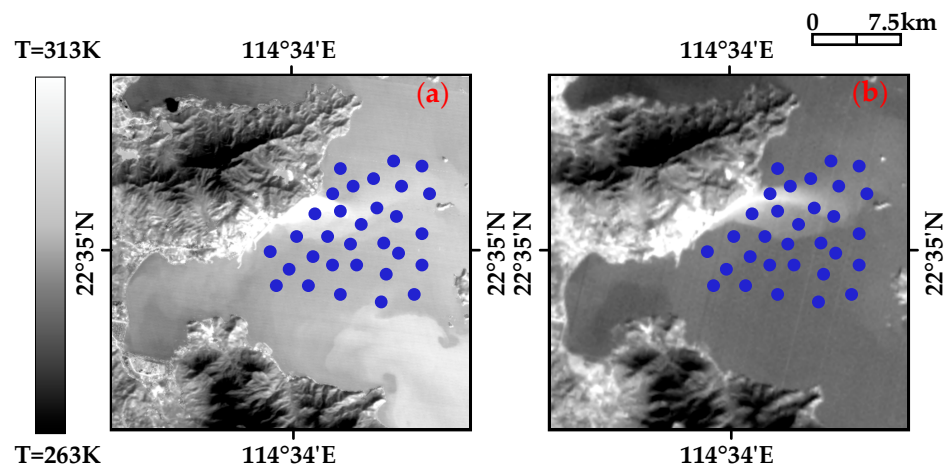


Figure 11. Spatial distribution of the 31 sampling points from the LA NPP (a) TIS (b) TIRS.

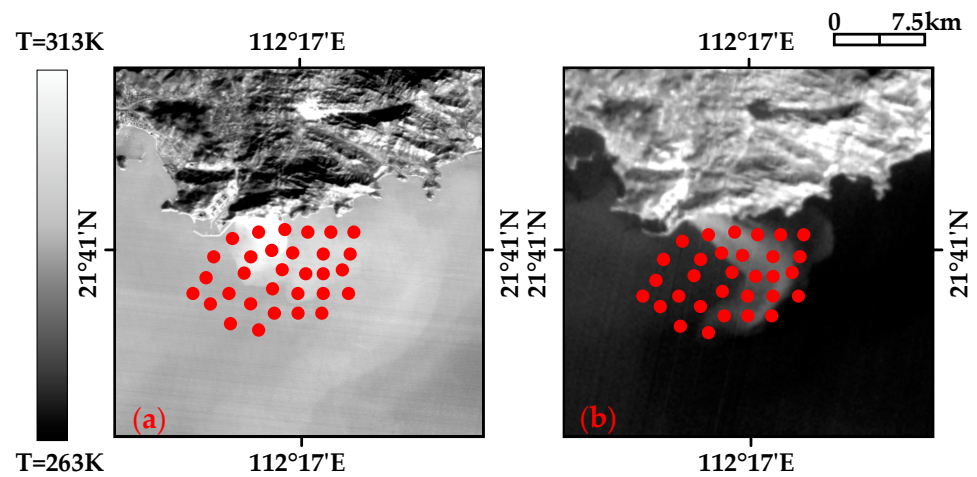


Figure 12. Spatial distribution of the 31 sampling points from the YJ NPP (a) TIS (b) TIRS.

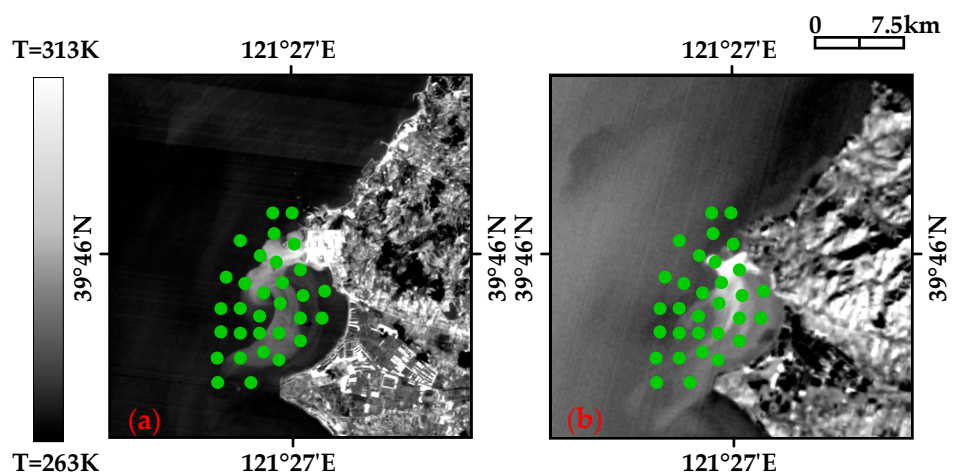


Figure 13. Spatial distribution of the 31 sampling points from the HY NPP (a) TIS (b) TIRS.

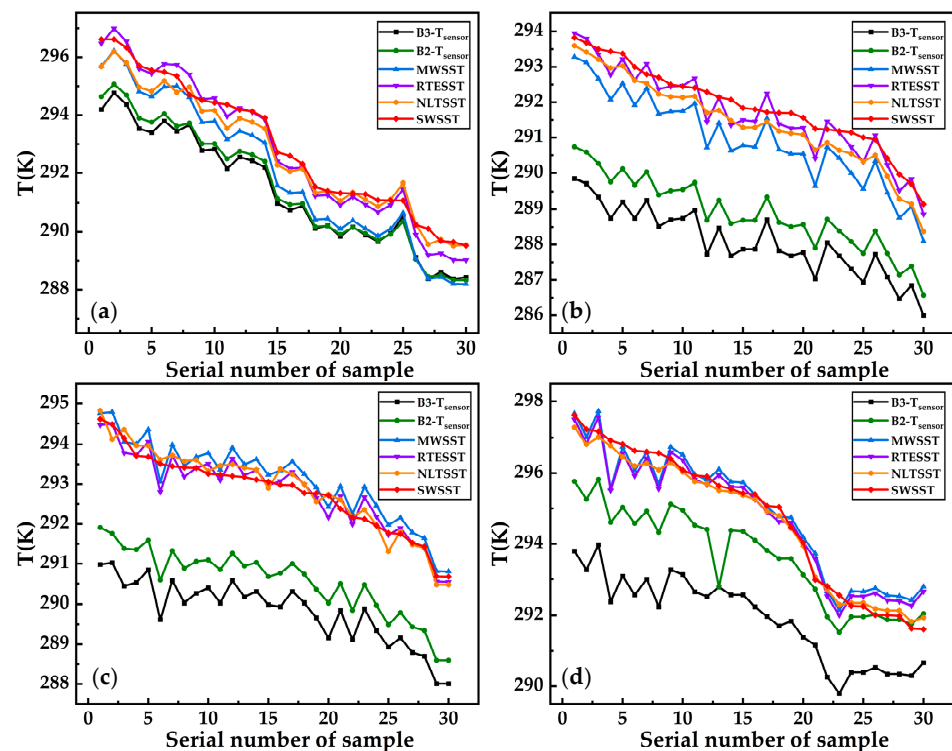


Figure 14. The comparisons of B2/B3 bright temperature, MWSST, RTE SST, NLSST, and SWSST of the 31 sampling points around the four NPPs: (a) TW NPP; (b) LA NPP; (c) YJ NPP; (d) HY NPP.

The Experimental results show the following:

- (1) MWSST, RTE SST, NLSST, and SWSST are all higher than B2/B3- T_{sensor} by about 3–5 °C.
- (2) The SST retrieved from the split-window algorithms (SWSST and NLSST) is generally higher than that of the single-channel algorithms (MWSST and RTE SST), which is largely related to the fact that the split-window algorithms can correct atmospheric effect and obtain more accurate SST.
- (3) The values of SWSST and NLSST are close to each other, with a small difference of 0.5 °C. It is inferred that the small difference is relevant to the NLSST algorithm's empirical coefficients, which have not been updated for a long time. The small difference also confirms the theoretical hypothesis stated in Section 2.4.4, which relatively verifies the accuracy of the SW algorithm.

3.2.3. Thermal Discharge Monitoring

As shown in Figures 15–18, five different colors are used to mark the temperature rise levels retrieved from the TW NPP, LA NPP, YJ NPP, and HY NPP TIS images under different months. Afterwards, the number of pixels and the acreage occupied by different temperature rise levels are calculated (the corresponding acreage of a single pixel is 30 m × 30 m). As shown in Figure 19, the statistical analysis shows that:

- (1) Obvious seasonal variation of the temperature rise area is monitored near the outfall of the four NPPs. The proportion of L1 temperature rise area is the largest (about 15 km² in winter and 5 km² in summer) and the smallest proportion is the L4 area (about 2 km² in winter and 0.5 km² in summer).
- (2) The highest temperature difference is about 4 °C, and the total acreage of temperature rise area is about 25 km², diffusing in a feather-shape to distant natural seas.
- (3) The temperature rise areas of different NPPs have obvious distinctions influenced by terrain, climate, wind direction, tides, and geographical location.

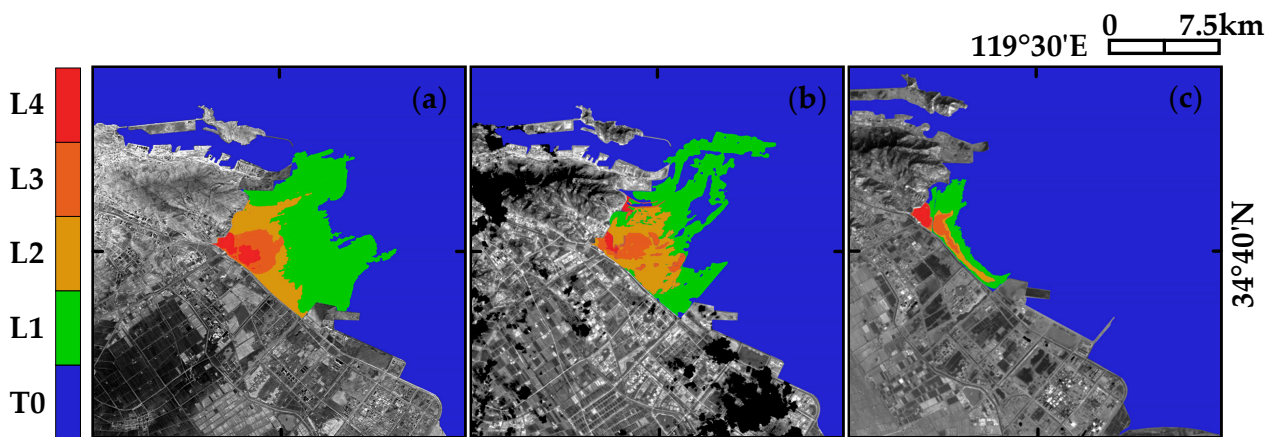


Figure 15. The temperature rise distribution of the TW NPP under different months: (a) 17 May 2022; (b) 11 September 2022; (c) 27 January 2023.

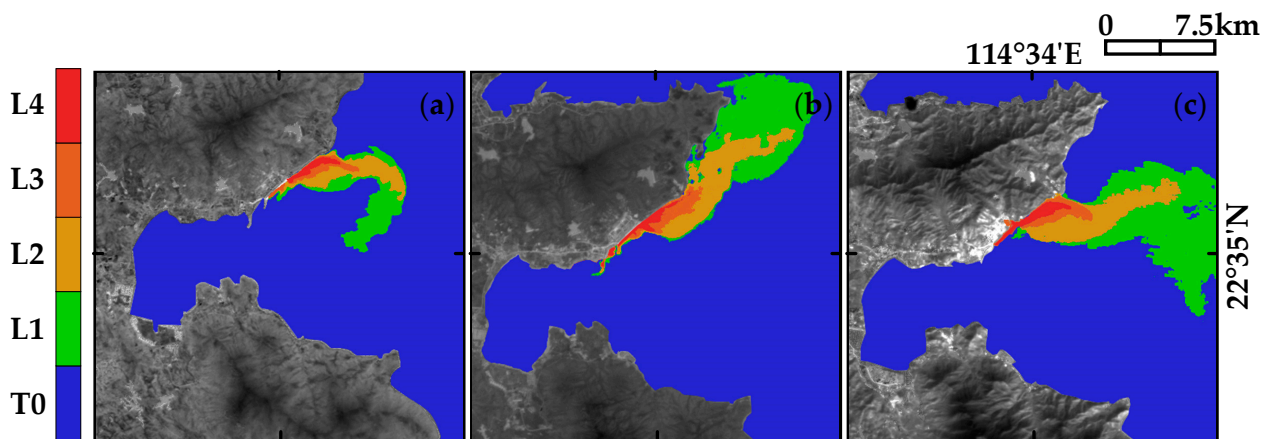


Figure 16. The temperature rise distribution of the LA NPP under different months: (a) 7 March 2022; (b) 12 July 2022; (c) 21 December 2022.

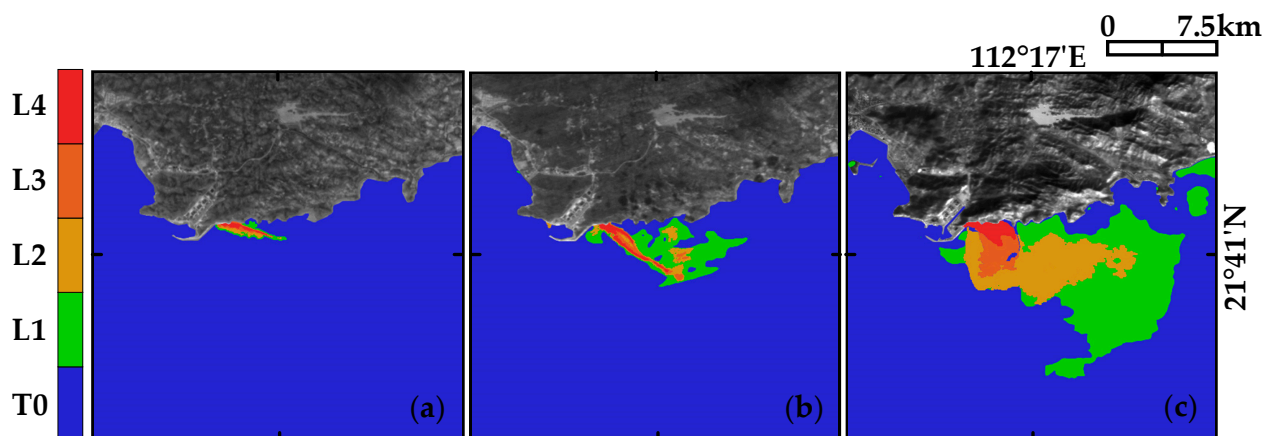


Figure 17. The temperature rise distribution of the YJ NPP under different months: (a) 22 July 2022; (b) 27 August 2022; (c) 11 December 2022.

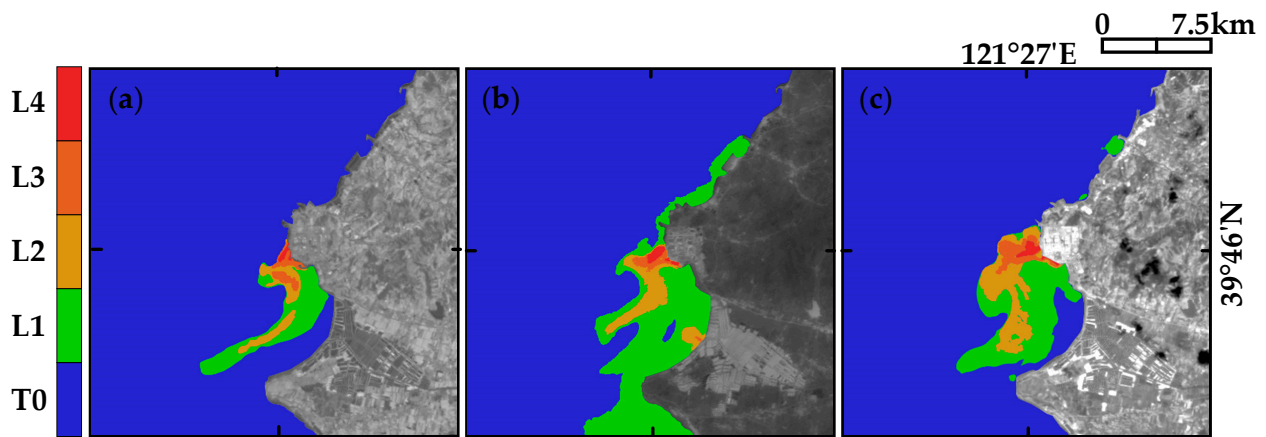


Figure 18. The temperature rise distribution of the HY NPP under different months: (a) 2 May 2022; (b) 29 June 2022; (c) 11 September 2022.

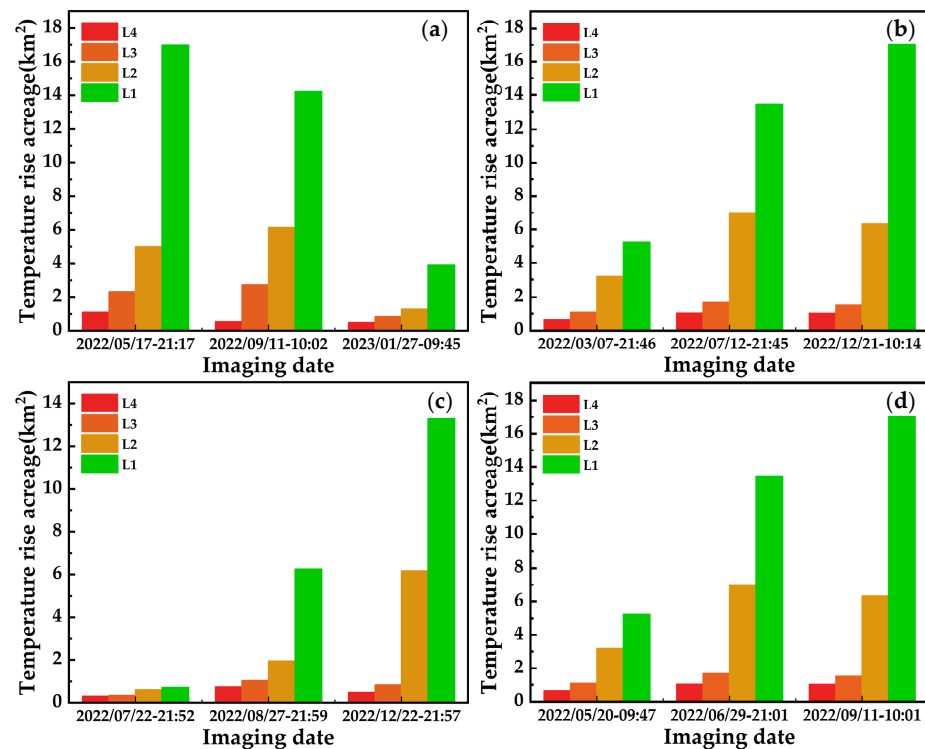


Figure 19. Column chart of acreage occupied by different temperature rise levels at the four NPPs: (a) TW NPP; (b) LA NPP; (c) YJ NPP; (d) HY NPP.

4. Conclusions

In this paper, we propose a simplified split-window-based temperature retrieval method (SW method) that is suitable for SDGSAT-1 TIS RSIs and which needs only atmospheric transmissivity and surface emissivity by counteracting the average atmospheric temperature. We quantitatively retrieve the SST of the TW NPP, LA NPP, YJ NPP, and HY NPP with thermal infrared RSIs from the SDGSAT-1 TIS and Landsat-8 TIRS. The TIS images (30 m) can depict more prominent boundary and clearer details than the TIRS images (100 m) because of higher spatial resolution. The SST retrieved from the split-window algorithms (SSWSST and NLSST) is generally higher than that of the single-channel algorithms (MWSST and RTESSST), which is largely related to the fact that the split-window algorithms can correct atmospheric effect and obtain more accurate SST. The obvious seasonal variations in the temperature rise area are monitored near the outfall of the four NPPs. Through

the above research, we find that the SDGSAT-1 TIS images can better describe the detailed distribution of thermal discharge based on the SW method, which provides a feasible and efficient method to monitor thermal pollution in small-scale regions. However, there are some uncertain factors in the retrieval process, including water and gas absorption, cloud coverage, mixed pixels, and proximity effect, which may cause some deviations in the retrieval results. Preprocessing of thin clouds can restore real surface information and reduce retrieval errors, which is an essential link in remote sensing analysis and application. Therefore, accurate atmospheric correction and cloud detection preprocessing are also important steps in the future optimization of thermal discharge monitoring.

Author Contributions: Conceptualization, W.H. and X.P.; methodology, W.H.; software, W.H. and L.Y.; validation, X.P. and W.H.; formal analysis, W.H.; investigation, W.H. and L.Z.; resources, F.C. and X.L.; data curation, Z.H. and X.L.; writing—original draft preparation, W.H.; writing—review and editing, W.H. and J.J.; visualization, W.H.; supervision, Z.H. and X.L.; project administration, F.C.; funding acquisition, F.C. All authors have read and agreed to the published version of the manuscript.

Funding: This research was funded by the Strategic Priority Research Program of the Chinese Academy of Sciences, grant number XDA19010102, and the National Natural Science Foundation of China under grant number 61975222.

Data Availability Statement: Not applicable.

Acknowledgments: The authors would like to thank the SDG BIGDATA Center and National Space Science Center for providing us with data.

Conflicts of Interest: The authors declare no conflict of interest.

References

1. Gaeta, M.G.; Samaras, A.G.; Archetti, R. Numerical investigation of thermal discharge to coastal areas: A case study in South Italy. *Environ. Model. Softw.* **2020**, *124*, 104596. [[CrossRef](#)]
2. Donlon, C.; Minnett, P.; Gentemann, C.; Nightingale, T.; Barton, I.; Ward, B.; Murray, M. Toward improved validation of satellite sea surface skin temperature measurements for climate research. *J. Clim.* **2002**, *15*, 353–369. [[CrossRef](#)]
3. Schluessel, P.; Emery, W.J.; Grassl, H.; Mammen, T. On the bulk-skin temperature difference and its impact on satellite remote sensing of sea surface temperature. *J. Geophys. Res. Ocean.* **1990**, *95*, 13341–13356. [[CrossRef](#)]
4. Fox-Kemper, B.; Hewitt, H.; Xiao, C.; Aðalgeirsdóttir, G.; Drijfhout, S.; Edwards, T.; Golledge, N.; Hemer, M.; Kopp, R.; Krinner, G. Ocean, cryosphere and sea level change. *AGU Fall Meet. Abstr.* **2021**, *2021*, U13B-09.
5. Zhang, Z.; Wang, D.; Cheng, Y.; Gong, F. Long-term changes and factors that influence changes in thermal discharge from nuclear power plants in Daya Bay, China. *Remote Sens.* **2022**, *14*, 763. [[CrossRef](#)]
6. Wang, X.; Gong, C.; Hu, Y.; Wang, X.; Li, L.; He, Z. Retrieval of sea surface temperature and thermal discharge monitoring in nuclear power plant using Gaofen-5 satellite remote sensing imagery. *J. Appl. Remote Sens.* **2022**, *16*, 012013. [[CrossRef](#)]
7. Tang, D.; Kester, D.R.; Wang, Z.; Lian, J.; Kawamura, H. AVHRR satellite remote sensing and shipboard measurements of the thermal plume from the Daya Bay, nuclear power station, China. *Remote Sens. Environ.* **2003**, *84*, 506–515. [[CrossRef](#)]
8. Chen, C.; Shi, P.; Mao, Q. Application of remote sensing techniques for monitoring the thermal pollution of cooling-water discharge from nuclear power plant. *J. Environ. Sci. Health Part A* **2003**, *38*, 1659–1668. [[CrossRef](#)]
9. Chelton, D.B.; Wentz, F.J. Global microwave satellite observations of sea surface temperature for numerical weather prediction and climate research. *Bull. Am. Meteorol. Soc.* **2005**, *86*, 1097–1116. [[CrossRef](#)]
10. Minnett, P.J.; Barton, I.J. Remote sensing of the earth's surface temperature. *Radiom. Temp. Meas. II Appl.* **2010**, *43*, 333–391.
11. Szczodrak, M.D.; Minnett, P.J. Relative Merits of Optimal Estimation and Non-Linear Retrievals of Sea-Surface Temperature from MODIS. *Remote Sens.* **2022**, *14*, 2249. [[CrossRef](#)]
12. Walton, C.C. Nonlinear multichannel algorithms for estimating sea surface temperature with AVHRR satellite data. *J. Appl. Meteorol. Climatol.* **1988**, *27*, 115–124. [[CrossRef](#)]
13. Dash, P.; Göttsche, F.-M.; Olesen, F.-S.; Fischer, H. Separating surface emissivity and temperature using two-channel spectral indices and emissivity composites and comparison with a vegetation fraction method. *Remote Sens. Environ.* **2005**, *96*, 1–17. [[CrossRef](#)]
14. Nie, P.; Zhu, H.; Xu, H.; Huang, Y.; Hua, W. Monitoring of Tianwan Nuclear Power Plant Thermal Pollution Based on Remotely Sensed Landsat Data. In Proceedings of the IGARSS 2020-2020 IEEE International Geoscience and Remote Sensing Symposium, Waikoloa, HI, USA, 26 September–2 October 2020; pp. 5624–5627.
15. Zhang, J.; Li, X.; Li, L.; Sun, P.; Su, X.; Hu, T.; Chen, F. Lightweight U-Net for cloud detection of visible and thermal infrared remote sensing images. *Opt. Quantum Electron.* **2020**, *52*, 397. [[CrossRef](#)]

16. Minnett, P.; Alvera-Azcárate, A.; Chin, T.; Corlett, G.; Gentemann, C.; Karagali, I.; Li, X.; Marsouin, A.; Marullo, S.; Maturi, E. Half a century of satellite remote sensing of sea-surface temperature. *Remote Sens. Environ.* **2019**, *233*, 111366. [CrossRef]
17. Wick, G.A.; Jackson, D.L.; Castro, S.L. Assessing the ability of satellite sea surface temperature analyses to resolve spatial variability—The northwest tropical Atlantic ATOMIC region. *Remote Sens. Environ.* **2023**, *284*, 113377. [CrossRef]
18. Tanahashi, S.; Kawamura, H.; Matsuura, T.; Takahashi, T.; Yusa, H. Improved estimates of wide-ranging sea surface temperature from GMS S-VISSR data. *J. Oceanogr.* **2000**, *56*, 345–358. [CrossRef]
19. Wu, Y.; Tang, F.; Dai, Y.; Wang, F.; Shi, Y.; Zhang, S. Blend with the Sea Surface Temperature from Different Satellites and Their Comparison in the Southeast Pacific Ocean. *J. Ocean Univ. China* **2023**, *22*, 452–458. [CrossRef]
20. Merchant, C.J.; Le Borgne, P. Retrieval of sea surface temperature from space, based on modeling of infrared radiative transfer: Capabilities and limitations. *J. Atmos. Ocean. Technol.* **2004**, *21*, 1734–1746. [CrossRef]
21. Embury, O.; Merchant, C.J.; Filipiak, M.J. A reprocessing for climate of sea surface temperature from the along-track scanning radiometers: Basis in radiative transfer. *Remote Sens. Environ.* **2012**, *116*, 32–46. [CrossRef]
22. Xuejiao, C.; Yunzhi, C. Mono-window Algorithm Applicability in Fujian Sea and Its Surrounding Areas Sea Surface Temperature Retrieval. *Remote Sens. Technol. Appl.* **2017**, *32*, 773–779.
23. Jiménez-Muñoz, J.C.; Sobrino, J.A. A generalized single-channel method for retrieving land surface temperature from remote sensing data. *J. Geophys. Res. Atmos.* **2003**, *108*, 4688. [CrossRef]
24. Fu, J.; Chen, C.; Guo, B.; Chu, Y.; Zheng, H. A split-window method to retrieving sea surface temperature from Landsat 8 thermal infrared remote sensing data in offshore waters. *Estuar. Coast. Shelf Sci.* **2020**, *236*, 106626. [CrossRef]
25. McMillin, L.M. Estimation of sea surface temperatures from two infrared window measurements with different absorption. *J. Geophys. Res.* **1975**, *80*, 5113–5117. [CrossRef]
26. McMillin, L.; Crosby, D. Theory and validation of the multiple window sea surface temperature technique. *J. Geophys. Res. Ocean.* **1984**, *89*, 3655–3661. [CrossRef]
27. Qin, Z.-H.; Zhang, M.-H.; Karnieli, A.; Berliner, P. Mono-window algorithm for retrieving land surface temperature from Landsat TM6 data. *Acta Geogr. Sin.* **2001**, *56*, 456–466.
28. Hanyue, C.; Li, Z.; Jiaguo, L.; Xieyu, F. A comparison of two mono-window algorithms for retrieving sea surface temperature from Landsat8 data in coastal water of Hongyan River nuclear power station. *Remote Sens. Nat. Resour.* **2018**, *30*, 45–53.
29. Kleespies, T.J.; McMillin, L.M. *Determination of Precipitable Water with the AVHRR (Advanced Very High Resolution Radiometer)*; Air Force Geophysics Lab Hanscom AFB MA: Bedford, MA, USA, 1988.
30. Hulley, G.C.; Hook, S.J. Generating Consistent Land Surface Temperature and Emissivity Products between ASTER and MODIS Data for Earth Science Research. *Geosci. Remote Sens. IEEE Trans.* **2011**, *49*, 1304–1315. [CrossRef]
31. Gillespie, A.; Rokugawa, S.; Matsunaga, T.; Cothorn, J.S.; Hook, S.; Kahle, A.B. A temperature and emissivity separation algorithm for Advanced Spaceborne Thermal Emission and Reflection Radiometer (ASTER) images. *IEEE Trans. Geosci. Remote Sens.* **1998**, *36*, 1113–1126. [CrossRef]
32. Li, L.; Jiang, L.; Zhang, J.; Wang, S.; Chen, F. A complete YOLO-based ship detection method for thermal infrared remote sensing images under complex backgrounds. *Remote Sens.* **2022**, *14*, 1534. [CrossRef]
33. Li, X.; Yang, L.; Su, X.; Hu, Z.; Chen, F. A correction method for thermal deformation positioning error of geostationary optical payloads. *IEEE Trans. Geosci. Remote Sens.* **2019**, *57*, 7986–7994. [CrossRef]
34. Planck, M. *The Theory of Heat Radiation*. 1914. Available online: <https://archive.org/details/theoryofheatradi00planrich> (accessed on 21 February 2023).
35. Marcq, S.; Delogu, E.; Chapelier, M.; Vidal, T.H. DirecTES: A Direct Method for Land and Sea Surface Temperature and Emissivity Separation for Thermal Infrared Sensors—Application to TRISHNA and ECOSTRESS. *Remote Sens.* **2023**, *15*, 517. [CrossRef]
36. Verdin, J.; Funk, C.; Klaver, R.; Roberts, D. Exploring the correlation between Southern Africa NDVI and Pacific sea surface temperatures: Results for the 1998 maize growing season. *Int. J. Remote Sens.* **1999**, *20*, 2117–2124. [CrossRef]
37. Srivastava, A.; Rodriguez, J.F.; Saco, P.M.; Kumari, N.; Yetemen, O. Global Analysis of Atmospheric Transmissivity Using Cloud Cover, Aridity and Flux Network Datasets. *Remote Sens.* **2021**, *13*, 1716. [CrossRef]
38. Wan, Z.; Li, Z.-L. A physics-based algorithm for retrieving land-surface emissivity and temperature from EOS/MODIS data. *IEEE Trans. Geosci. Remote Sens.* **1997**, *35*, 980–996.
39. Shi, H.; Xiao, Z.; Wen, J.; Wu, S. An Optical–Thermal Surface–Atmosphere Radiative Transfer Model Coupling Framework with Topographic Effects. *IEEE Trans. Geosci. Remote Sens.* **2020**, *60*, 1–12. [CrossRef]
40. Zhu, H.; Li, Q.; Zheng, C.; Hong, Y.; Xu, Z.; Wang, H.; Shen, W.; Kaur, S.; Ghosh, P.; Qiu, M. High-temperature infrared camouflage with efficient thermal management. *Light Sci. Appl.* **2020**, *9*, 60. [CrossRef] [PubMed]
41. Petrenko, B.; Ignatov, A.; Kihai, Y.; Stroup, J.; Dash, P. Evaluation and selection of SST regression algorithms for JPSS VIIRS. *J. Geophys. Res. Atmos.* **2014**, *119*, 4580–4599. [CrossRef]
42. Chen, Y.; Duan, S.-B.; Labeled, J.; Li, Z.-L. Development of a split-window algorithm for estimating sea surface temperature from the Chinese Gaofen-5 data. *Int. J. Remote Sens.* **2019**, *40*, 1621–1639. [CrossRef]

Disclaimer/Publisher’s Note: The statements, opinions and data contained in all publications are solely those of the individual author(s) and contributor(s) and not of MDPI and/or the editor(s). MDPI and/or the editor(s) disclaim responsibility for any injury to people or property resulting from any ideas, methods, instructions or products referred to in the content.